Influence of Microstructure and Droplet Volume on Atmospheric Pitting Corrosion of 304L Austenitic Stainless Steel

Sarkat R. Hussein† and Haval B. Mohammed-Ali

Department of Physics, College of Science, University of Zakho, Zakho, Kurdistan Reign – F.R. Iraq

***Abstract*—This research investigates the atmospheric pitting corrosion behavior of 304L austenitic stainless steel subjected to $MgCl_2$ droplets, emphasizing the effects of microstructure and droplet volume. X-ray diffraction and scanning electron microscopy (SEM) show that both austenite and ferrite are present, and it is observed that the ferrite bands dissolved more in the direction the steel is rolled. SEM-energy-dispersive X-ray spectroscopy analysis identified mixed oxides and MnS inclusions. The shape of the pits changed depending on the direction of the plate: Layered pits mostly occurred on the longitudinal–transverse side, while striped pits are seen on the longitudinal–short transverse and short transverse sides, indicating variations in the material's structure. An increase in droplet volume from 0.5 μL to 2.5 μL led to a linear rise in total pit area and a measurable increase in pit depth. These findings show that the direction of the microstructure and the size of the droplets significantly affect how likely pitting is to occur, which is important for designing and using stainless steels in environments with a lot of chloride.**

***Index Terms*—Atmospheric pitting corrosion, Austenitic stainless steel, Droplet diameter, Inclusions, Microstructure.**

. Introduction

Stainless steels consist of many essential components sourced from the earth's crust, including iron ore, chromium, silicon, nickel, carbon, nitrogen, and manganese. Austenitic grades are designated by numbers in the 200 and 300 series, with the 300 series derived from the conventional stainless steel, including 18% chromium and 8% nickel (Kalpakjian and Schmid, 2006). The 300 series grades include "L" type machining of austenitic stainless steels (ASS), designed for enhanced corrosion resistance. The "L" signifies low carbon content, approximately 0.03%, as seen in 304L. This grade is ideal for a wide array of applications requiring superior corrosion resistance, along with excellent formability and weldability. It is often used in sectors, including food (encompassing cooking appliances, stoves, freezers, milk processing, wine manufacturing, and storage tanks), as well as in the petrochemical, chemical, and nuclear industries, the dyeing sector, architecture, and medicine (Zatkalíková and Markovičová, 2019; Liptáková, 2009). The management of "intermediate-level nuclear waste" in the United Kingdom is a significant concern for the nuclear waste sector, since it is currently housed in containers constructed from Type 304L ASS (Cheng, et al., 2017). Nonetheless, even with its natural passivity, 304L stainless steel is still prone to localized corrosion, especially pitting, when it comes into contact with environments high in chlorides, such as marine settings or industrial zones with airborne salts (Sedriks, 1996; Leygraf, et al., 2000).

A multitude of researchers have investigated the atmospheric corrosion of ASS (Cheng, et al., 2017; Van Nam, et al., 2015a; Schindelholz, Risteen and Kelly, 2014; Cruz, Nishikata and Tsuru, 1998; Maier and Frankel, 2010; Maier and Frankel, 2011; Tsutsumi, Nishikata and Tsuru, 2007; Mi, et al., 2011; Street, et al., 2018; Montoya, et al., 2023). In such steels, both austenitic and ferritic phases (delta-ferrite) can form. Having around 2–5% ferrite is advantageous in fully austenitic SS, since the ferrite phase enhances hot workability (Alberth, et al., 2006; Brooks, Thompson and Williams, 1984; Hull, 1967). However, the presence of such a small amount of delta ferrite was found to be detrimental to the microstructure of the alloy (Manning, Duquette and Savage, 1980; Donohoe, Whillock and Apps, 2012). Pitting was seen to correspond with the ferrite bands on the (LS) and (ST) orientations of 304L SS, penetrating the pit through air corrosion, so proving that ferrite orientation significantly affects the morphologies of atmospheric pits (Mohammed-Ali, et al., 2018). Therefore, there is a need for more investigation of such influence for the ASSs.

It is well recognized that inclusions, such as MnS and mixed oxides on the stainless-steel surface serve as beginning sites for pitting corrosion (Schmuki, et al., 2005; Webb and Alkire, 2002a; Webb and Alkire, 2002b; Park, Matsch and Böhni, 2001; Williams and Zhu, 2000; Ryan, et al., 2002).

ARO-The Scientific Journal of Koya University
Vol. XIII, No.2(2025), Article ID: ARO.12445.8 pages
DOI: 10.14500/aro.12445
Received: 17 July 2025; Accepted: 24 August 2025
Regular research paper; Published: 18 September 2025
†Corresponding author's e-mail: sarkat.hussein@staff.uoz.edu.krd

These inclusions can locally disrupt the passive film, serving as preferential sites for pitting under atmospheric and chloride-laden conditions (Nishimoto, Muto and Sugawara, 2023; Hu, et al., 2016). Elongated inclusions have been shown to be essential for pit initiation and growth in SS (Mohammed Ali, 2025). Mair and Frankel et al. (Maier and Frankel, 2010) also observed that.

The microstructure of stainless steel plays a crucial role in determining its resistance to localized corrosion. Microstructural features, such as grain boundaries, non-metallic inclusions, delta ferrite distribution, and residual stresses introduced during processing can lead to heterogeneous electrochemical behavior and passive film instability (Helbert, et al., 2022, Le, et al., 2008).

The diameter and volume of droplets have a profound effect on the corrosion process (Maier and Frankel, 2010; Tsutsumi, Nishikata and Tsuru, 2007; Mohammed Ali, 2016; Mi, 2014). Smaller droplets tend to have limited buffering capacity and can experience more extreme local pH and chloride concentration shifts as they evaporate. This creates highly localized and aggressive environments that favor pit nucleation. Research has shown that pit initiation under small droplets occurs more frequently and rapidly than under larger ones due to the intensification of local chemistry (Tsutsumi, Nishikata and Tsuru, 2007). In addition, droplet confinement can restrict oxygen diffusion, leading to the establishment of differential aeration cells that further drive localized attack.

This work examined atmosphere pitting corrosion under $MgCl_2$ droplets using SEM and optical microscopy in laboratory trials to investigate the influence of microstructure and droplet area on Type 304L ASS.

. Experimental Method

A. Material and Sample Preparation

Type 304L, an austenitic SS plate, was obtained from "Aperam, France." The alloy, referred to as the "as-received" sample, was cold-rolled and then cooled using forced air by the manufacturer. The alloy's chemical makeup (in weight percent) is as follows: chromium (Cr) 18–19.5%, nickel (Ni) 8–10.5%, manganese (Mn) 2%, sulfur (S) 0.015%, carbon (C) 0.03%, silicon (Si) 0.75%, nitrogen (N) 0.1%, and phosphorus (P) 0.045%, with iron (Fe) comprising the remainder. Fig. 1 depicts the sample orientations: The top surface (longitudinal–transverse [LT]), side grain (longitudinal–short transverse [LS]), and end grain (short transverse [ST]). Samples were sectioned in the rolling direction (RD) with dimensions of 20 × 25 mm for LT and 3 × 20 mm for both LS and ST, all maintaining a consistent thickness of 3 mm.

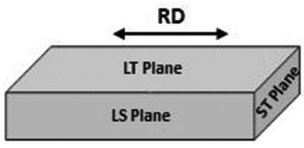

Fig. 1. Plate orientations and the rolling direction.

B. Lab-Based Droplet Experiments

The specimens were cold-mounted and oriented to display the top surface plane (LT), side grain (LS), and end grain (ST) planes to evaluate the impact of three plate orientations. 304L specimens were ground using 800-grit SiC paper, then splashed with deionized water (DI), ultrasonically cleaned with DI water for 10–5 min, and finally had their surfaces dried with cold air before any tests were conducted. Following that, the specimens spent a whole day in a desiccator in the open air for the passive film to establish before the droplet deposition.

C. Droplet Deposition

Magnesium chloride hexahydrate ($MgCl_2 \cdot 6H_2O$), which was acquired from HIMEDIA, was dissolved in deionized (DI) water to create the salt solution. The pH of the $MgCl_2$ solution is in the mildly acidic range, approximately 5–6, depending on concentration and temperature. For droplet deposition, a micropipette with a volume range of 0.5–2.5 μL and an accuracy of 0.81% was used. Four specimens were prepared: Three specimens had side grain (LS), end grain (ST), and surface (LT) orientations, each deposited with 1 μl droplets of 0.4 M of magnesium chloride ($MgCl_2$) (Fig. 2a-c). It took around 4–5 min to deposit twenty-four drops on the surface (LT). The fourth specimen was the surface (LT), which had variant droplet volumes as shown in Fig. 2d. Using FIJI/ImageJ software, the area of each droplet was determined. The chloride deposition density (CDD) was estimated to be around 800–1570 μg/cm^2. The exposure time of the tests was selected to be 1 week.

D. Regulation of Relative Humidity (RH) and Temperature

RH was regulated throughout the atmospheric corrosion testing using saturated salt solutions. Magnesium chloride hexahydrate ($MgCl_2 \cdot 6H_2O$) was used to sustain a RH of 35% (ASTM, 1985), with an effective temperature range of 5–80°C (ASTM, 1985). During every test, the solutions were kept in covered desiccators. We used a data logger (EL-21CFR-2-LCD, Lascar Electronics) to track temperature and humidity. After that, the desiccators were put within an environmental chamber (NLF64–320) that kept the temperature at 30 ± 1°C.

E. Microstructural Examination

The plate was divided into three orientations using cutting wheels: The top surface (LT) plane measured 25 × 20 mm, while the side grain (LS) and end grain (ST) planes measured 20 × 3 mm. To investigate the impact of microstructure, all samples were manufactured and mounted in Bakelite. 800-grit SiC paper was used to grind the specimens, and then water-based monocrystalline diamond solutions with sizes of 6 μm, 3 μm, and 1 μm were used to polish them. At room temperature (around 20°C), etching was done for up to 5 s using Kaling's No. 2 reagent (5 g $CuCl_2$, 100 mL HCl, and 100 mL ethanol). The base alloy's microstructure was inspected, and its chemical composition was determined using an energy-dispersive X-ray spectroscopy (EDX) equipped scanning electron microscope (SEM, Quanta 450). The

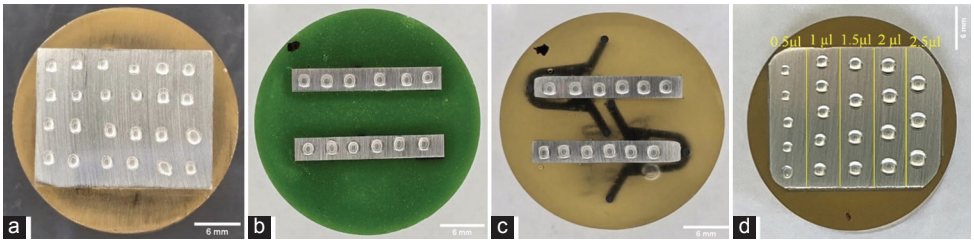

Fig. 2. Type 304L austenitic stainless steel with deposited $MgCl_2$ droplets**:** (a) The surface (longitudinal–transverse [LT]), (b) side grain (longitudinal–short transverse), (c) end grain (short transverse) orientations, and (d) the surface (LT) with the variant droplet volumes.

existence of austenite and ferrite phases was also determined by X-ray diffraction (XRD) investigation utilizing an analytical X' Pert PRO diffractometer (Cu Kα, λ = 1.5406 Å).

F. Measurement of the Pit Depth and Pit Mouth Area

An optical microscope was used to measure the depth of each identified pit. The disparity between the top surface and the bottom of the pits was measured using an optical microscope to ascertain the depth of the pits by ASTM guidelines (Standard, 2005).

For the pit mouth measurement, each pit was photographed using the optical microscope. The wand tool in the FIJI/ImageJ application was used to quantify the pit area, similarly to droplet area analysis. Using a tolerance value of 40, the wand tool was used to choose the edge of each pit. Following selection, the area was calculated using the "Measure" function. To make additional computations easier, these area values were then transformed into comparable diameters using the formula $A = \varpi r^2$, supposing that each pit had a roughly circular shape.

□. Results and Discussion

A. Microstructural Characterization

Fig. 3 displays the acquired LT specimen of ASS 304L's XRD patterns. The seven peaks consist of the two fundamental phases, γ austenite and α ferrite. It is well agreed that α ferrite is present in a small percentage in ASSs (Mohammed-Ali, et al., 2018). The austenite and delta ferrite phases may be identified and measured using XRD. However, there are several limitations on the application of XRD, including the minimum volume needed to generate a sufficiently strong signal (usually 5% volume [Tavares, Fruchart and Miraglia, 2000]). Moreover, XRD may be impacted by orientation issues (Zhang, et al., 2000). The little delta ferrite signal in the XRD data indicates that the substance makes up at least 5% of the volume (Mohammed Ali, 2016).

Following polishing and a 5-s etching with Kalling's 2 reagent, SEM images of the three plate sides (LT, LS, and ST) of 304L SS are shown in Fig. 4. The bands dissolved more readily in the RD. These bands are analogous to ferrite bands, with the light gray area denoting (austenite) γ phases and the dark gray area representing ferrite (α) phases. Broader bands were seen in the LT side (Fig. 4a) (Mohammed Ali, 2016). The alloy's microstructure displayed austenite grains of

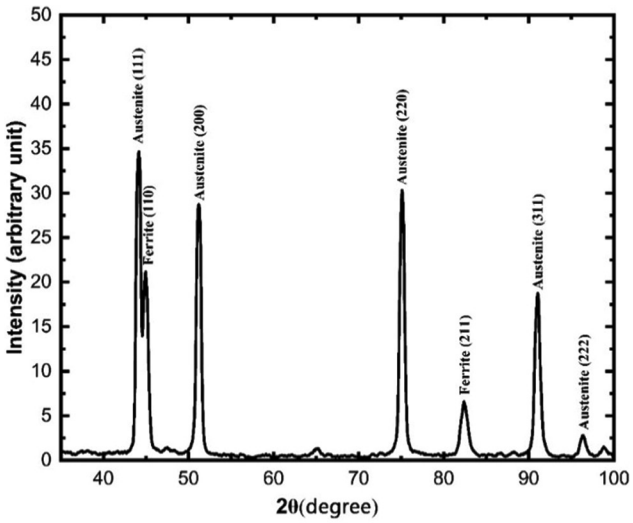

Fig. 3. X-ray diffraction pattern of type 304L stainless steel (longitudinal–transverse plane).

coarse equiaxed shape in three plate sides, accompanied by elongated ferrite bands, attributed to the pressing and rolling procedures during production (Mampuya, et al., 2021).

B. Inclusion Analysis

The characterization of inclusions on the LS side for the examined alloy was conducted using SEM with an EDX detector. Fig. 5 illustrates the SEM image of inclusions existing in the examined steel in this study. Two forms of inclusions were observed: Circular and elongated-like shape inclusions, as seen in Fig. 5a and b. At least three inclusions of each type were examined. An exemplary instance of mixed oxide incorporation on the LS plane is seen in Fig. 6, with three-point EDX scans across the inclusion marked as "1502," "1503," and "1505" compared with one one-point scan of the base metal marked as "1504" as indicated in the figure. EDX maps also succeeded in determining the chemical composition of this type of inclusion, as shown in Fig. 7. Other researchers also reported the presence of such inclusions in ASS (Ida, et al., 2024, Chiba, et al., 2012, Eguchi, 2023; Williams and Zhu, 2000).

C. Influence of Plate Orientation

The impact of three plate orientations on pit morphology was examined for the Type 304L austenitic SS alloy. Samples were examined after 1 week of exposure at 35%

http://dx.doi.org/10.14500/aro.12445

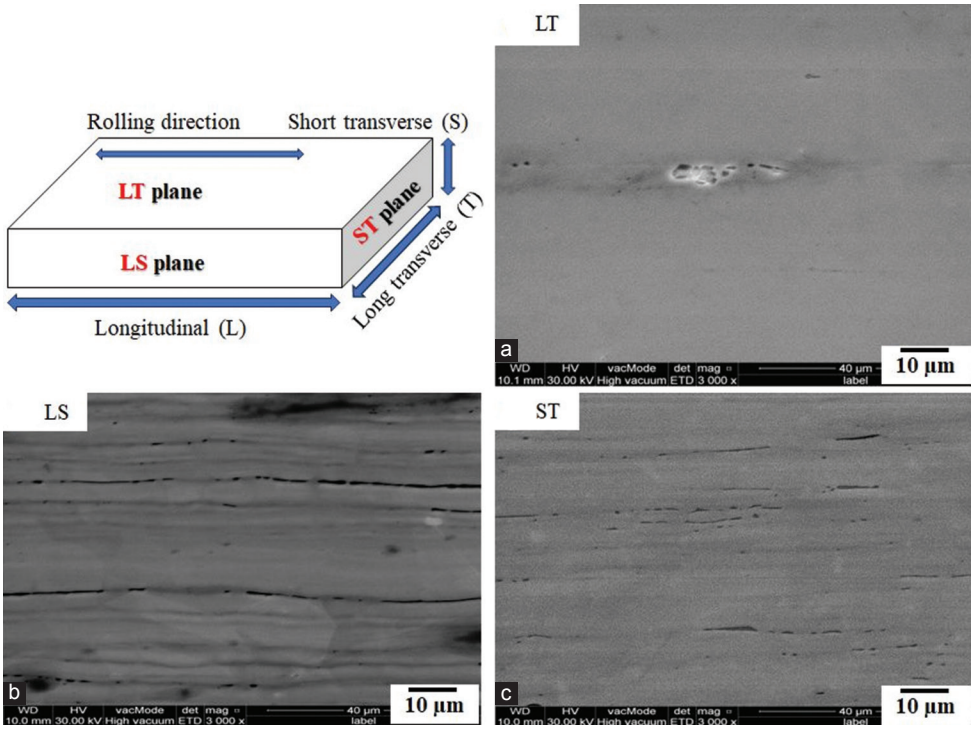

Fig. 4. The microstructure of the plate sides (longitudinal–transverse [LT], longitudinal–short transverse [LS], and short transverse [ST] sides) of the type 304L SS plate after 5 s of Kalling's 2 etching. (a) LT, (b) LS, (c) ST.

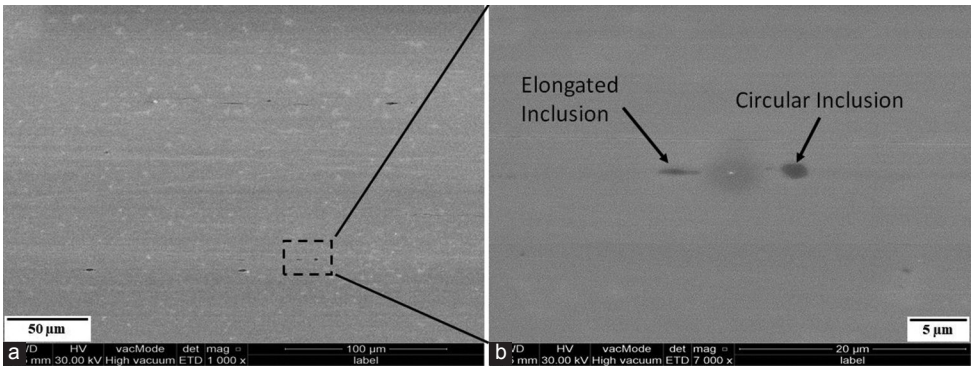

Fig. 5. (a) Type 304L stainless steel (longitudinal–short transverse plan) with inclusion, and (b) magnified section of (a).

RH. A minimum of 12 droplets were placed on the LS plane. An equivalent quantity was placed on the ST plane, all exhibiting the characteristics shown in Table □, while 24 droplets were formed on the LT plane. Twenty-one out of twenty-four droplets exhibited pitting (Table □), with eleven of them, including several pits designated as "satellite" pits (Street, et al., 2015; Mohammed Ali, 2016). The mechanism of the formation of such pits was described in terms of time-lapse in previous studies (Mohammed Ali, 2016; Street, et al., 2015). Two elongated pits were observed among the pits on the LS plane. This was attributed to the presence of the elongated inclusions on this plane (Guo, et al., 2019, Mohammed-Ali, et al., 2018; Mohammed-Ali 2025). The predominant occurrence on the ST plane was the creation of several pits.

Fig. 8 illustrates the morphology of pits formed on the LT, LS, and ST sides of the ASS plate orientations. The LS and ST sides exhibit a striped morphology of undissolved metal strands aligned with the RD, but the LT plate displays a layered attack pattern that seems to penetrate into the metal. The form of the observed pits and the microstructure of

TABLE I

SUMMARIZES CORROSION TEST FINDINGS AND THE PROBABILITY OF PITTING ON ASS 304L PLATE ORIENTATIONS UNDER 0.4M MGCL2 DROPLETS AND MATERIAL CONDITION AS RECEIVED, WHICH WAS MAINTAINED AT 30 °C±2, RH 33%±2.

Exposure time	Droplets volume (µL)	Orientation	CDD (µg/cm²)	Number of droplets pitted
1 week	1 µL	LT	1250	21/24
	1 µL	LS	1250	12/12
	1 µL	ST	1250	12/12
	0.5 µL	LT	800	4/5
	1 µL		1250	5/5
	1.5 µL		1355	4/4
	2 µL		1490	4/4
	2.5 µL		1570	3/3

CDD: Chloride deposition density

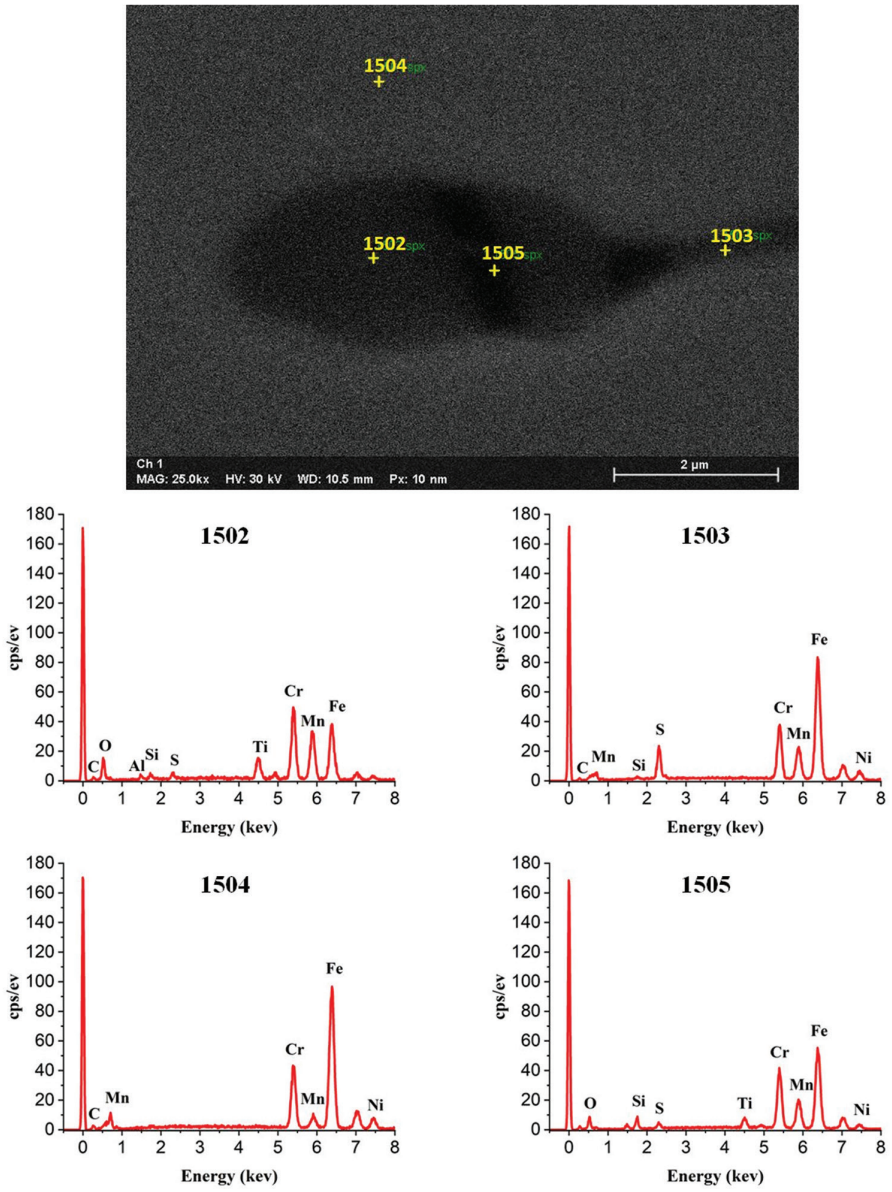

Fig. 6. Scanning electron microscopy image depicting form inclusions on the longitudinal–short transverse plane of type 304L austenitic stainless steels after final polishing, accompanied by an energy-dispersive X-ray spectroscopy scan of four spots exhibiting mixed oxide MnS inclusions.

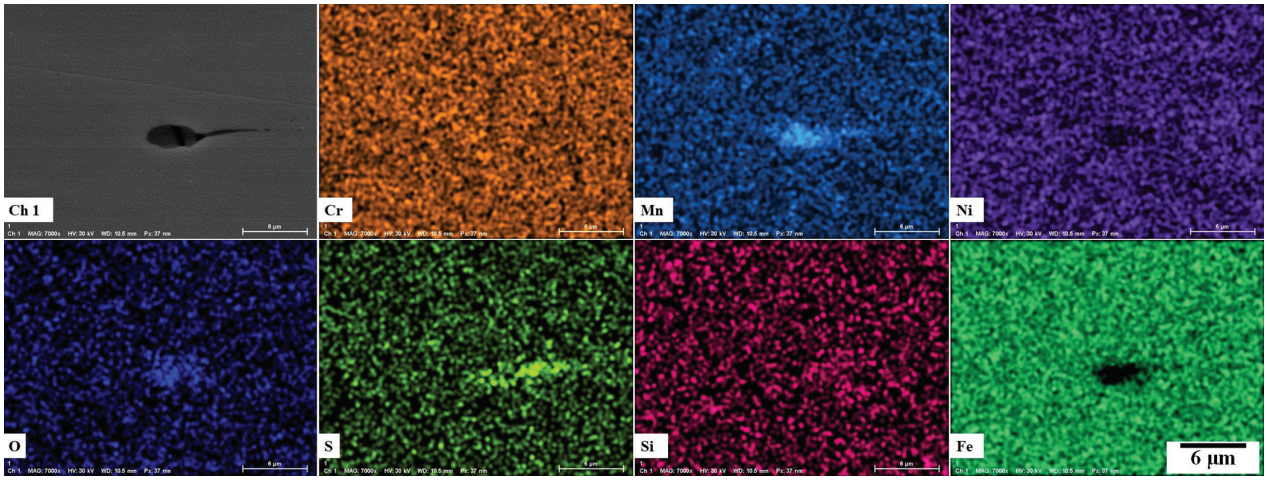

Fig. 7. Shows an enlarged scanning electron microscopy picture of a MnS inclusion identified on the longitudinal–short transverse side of the final polished base of type 304L austenitic stainless steels, accompanied by energy-dispersive X-ray spectroscopy analysis of the elemental map.

http://dx.doi.org/10.14500/aro.12445

the alloy are interconnected (refer to Figs. 4 and 8). These findings align with the results achieved by prior studies (Mohammed-Ali, et al., 2018). Preferential attack in ASS is often seen in either austenite or ferrite, contingent upon the air conditions dictated by the exposure circumstances and the material's characteristics (Mohammed-Ali, et al., 2018, Street, et al., 2015, Guo, et al., 2019).

Table □ summarizes corrosion test findings and the probability of pitting on ASS 304L plate orientations under 0.4 M $MgCl_2$ droplets and material condition as received, which was maintained at 30°C ± 2, RH 33% ± 2.

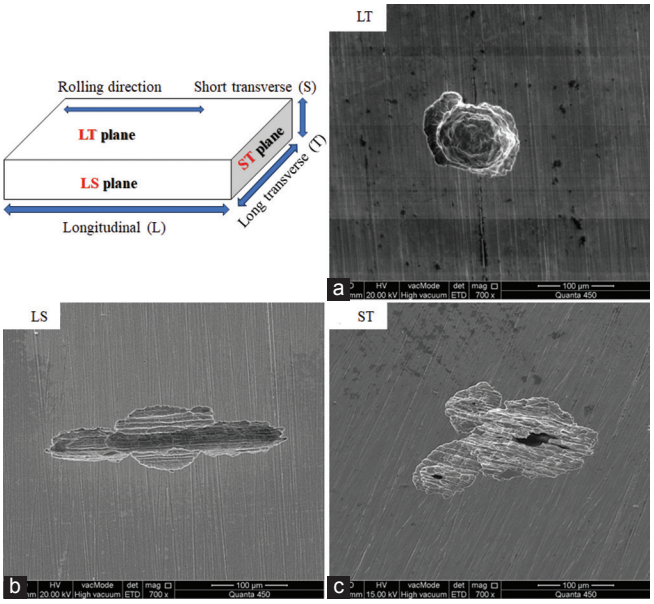

Fig. 8. Scanning electron microscopy pictures of pits developed on Type 304L SS plate during 1 week of exposure at 35% relative humidity and 30°C: (a) Longitudinal–transverse plane, (b) longitudinal–short plane, and (c) short–transverse plane.

D. Droplet Volume Effects

Fig. 9 illustrates the series of $MgCl_2$ droplets of different volumes on the surface of a 304L SS plate. The droplet volumes varied from 0.5, 1, 1.5, 2, to 2.5 µL, resulting in average droplet equivalent diameters of 1.5, 1.7, 2.0, 2.2, and 2.4 mm, with CDDs of 800, 1250, 1355, 1490, and 1570 µg/cm^2, respectively. This deposition approach was developed to examine how droplet size affects pit area and depth. In total, 20 out of 21 droplets were pitted. The results of this test are summarized in Table □. In this experiment, a solitary pit per droplet was the predominant occurrence for the 2.5 µL volume; however, both single-pits and multiple-pits (termed "satellite" pits) morphologies were seen at other volumes. Fig. 9 (b) illustrates the standard pit morphologies. All the pits had a shallow dish-like morphology, with one side much more eroded, resulting in a "earing shape" appearance (Street, et al., 2015; Maier and Frankel, 2010; Mohammed Ali, 2016), as seen in the standard SEM pictures, Fig. 9c. Street et al. (Street, et al., 2015) named such pit morphology as ''spiral'' pit morphology.

Fig. 10 demonstrates the influence of droplet volume on total pit area and pit depth. As the droplet volume escalated from 0.5 µL to 2.5 µL, both specified parameters demonstrated a steady rise. The total pit area increased significantly with larger droplet sizes, indicating that increased droplet volume promotes more extensive lateral corrosion. A particularly sharp increase was observed at the highest volume (2.5 µL), suggesting that larger droplets enhance

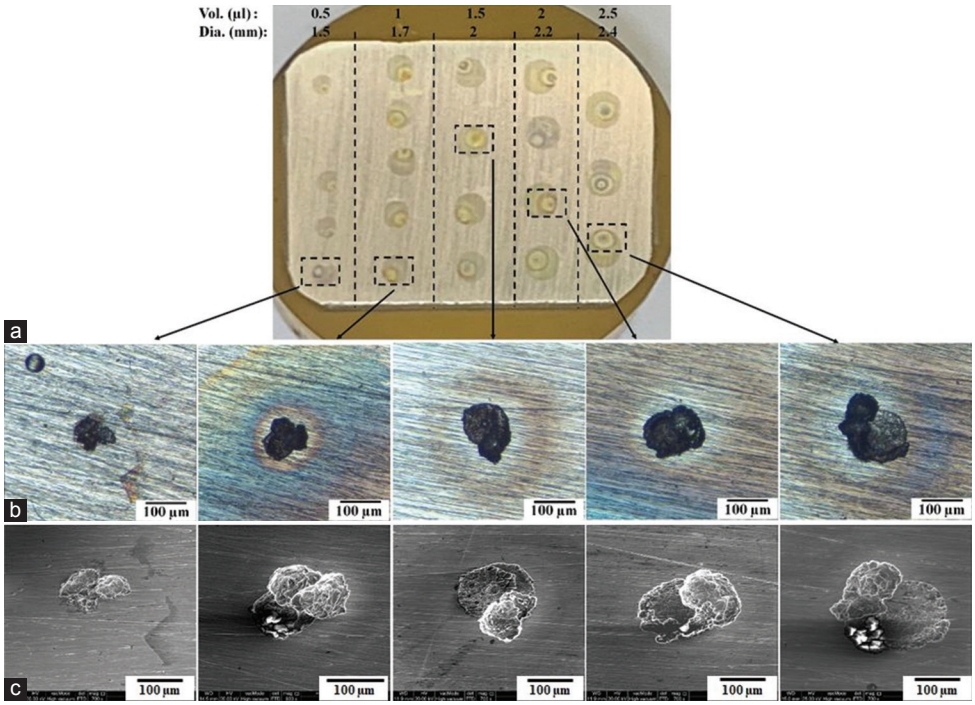

Fig. 9: (a) 304L SS plate surface deposited with $MgCl_2$ droplets of different volumes following exposure for 1 week following wash with deionized water; (b) optical micrographs of typical pits; (c) Scanning electron microscopy micrographs of pits shown in (b).

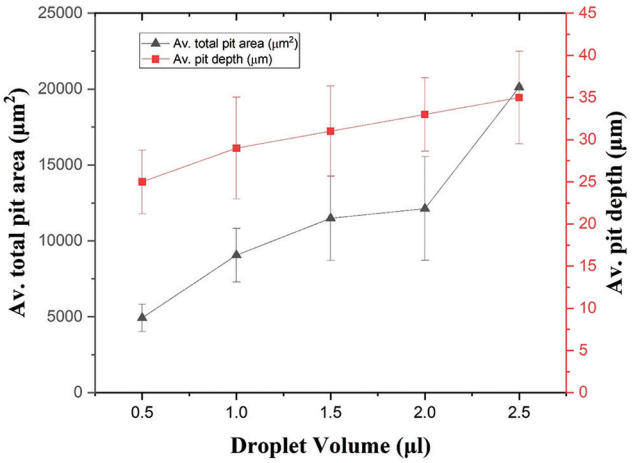

Fig. 10: The mean total pit area and mean depth as a function of droplet volume of 304L SS after 1 week at 35% relative humidity and 30°C.

electrolyte retention and prolong chloride exposure at the metal surface. Furthermore, as droplet volume increases, the amount of chloride deposited also rises, thereby intensifying the corrosion process (Tsutsumi, Nishikata and Tsuru, 2007; Van Nam, et al., 2015b; Maier and Frankel, 2010).

Similarly, average pit depth increased steadily with droplet volume, reflecting a more aggressive localized attack. This can be attributed to reduced evaporation rates in larger droplets, allowing for a more prolonged electrochemical reaction and stable anodic dissolution (Van Nam, et al., 2015b). This is due to an expansion in the "effective cathode area," which may result in a rise in potential (Tsutsumi, Nishikata and Tsuru, 2007, Mi, et al., 2011, Wang, et al., 2011, Chen and Kelly, 2007). However, at 43% RH, it has been shown that there is no discernible difference in pit depth (Mohammed Ali, 2016).

IV. Conclusion

This study investigated the effects of microstructure and droplet diameter on atmospheric pitting corrosion of ASS 304L under $MgCl_2$ droplets. Key findings include:

- The microstructure of the analyzed alloy comprises two phases: Austenite and ferrite, as shown by XRD and SEM. In addition, two categories of inclusions, namely, mixed oxide and MnS inclusions, were analyzed using SEM and EDX techniques.
- Pit morphology exhibited variation based on plate orientation, coinciding with the delta ferrite present in the microstructure. The LT plane had a stratified attack, while the LS and ST planes displayed a striped morphology with ferrite bands preferentially dissolved in the RD.
- Increasing droplet volume increased pit area and pit depth.

References

Alberth, M., Majoros, L., Kovalecz, G., and Borbas, E., 2006. Bibliography current world literature. *Oncology Research*, 12, pp.237-241.

ASTM Designation E., 1985. Standard practice for maintaining constant relative humidity by means of aqueous solutions. *ASTM Designation E,* 104-85, pp.790-795.

Brooks, J., Thompson, A., and Williams, J., 1984. A fundamental study of the beneficial effects of delta ferrite in reducing weld cracking. *Welding Journal,* 63, pp.71S-83S.

Chen, Z., and Kelly, R., 2007. An analytical modeling method for calculating the maximum cathode current deliverable by a circular cathode under atmospheric exposure. *WIT Transactions on Engineering Sciences*, 54, p.9.

Cheng, C.Q., Klinkenberg, L.I., Ise, Y., Zhao, J., Tada, E., and Nishikata, A., 2017. Pitting corrosion of sensitised type 304 stainless steel under wet-dry cycling condition. *Corrosion Science*, 118, pp.217-226.

Chiba, A., Muto, I., Sugawara, Y., and Hara, N., 2012. A microelectrochemical system for in situ high-resolution optical microscopy: Morphological characteristics of pitting at MnS inclusion in stainless steel. *Journal of the Electrochemical Society,* 159, p.C341.

Cruz, R.V., Nishikata, A., and Tsuru, T., 1998. Pitting corrosion mechanism of stainless steels under wet-dry exposure in chloride-containing environments. *Corrosion Science*, 40, pp.125-139.

Donohoe, C., Whillock, G., and Apps, P., 2012. Localized corrosion of stainless steel in a nuclear waste cooling water system-Part 2: Plant inspection findings. *Corrosion*, 68, pp.844-852.

Eguchi, K., 2023. Quantitative analysis of initiation site of pitting corrosion on type 304 austenitic stainless steel. *Corrosion Science*, 221, p.111312.

Guo, L., Street, S.R., Mohammed-Ali, H.B., Ghahari, M., Mi, N., Glanvill, S., Du Plessis, A., Reinhard, C., Rayment, T., and Davenport, A.J., 2019. The effect of relative humidity change on atmospheric pitting corrosion of stainless steel 304L. *Corrosion Science*, 150, pp.110-120.

Helbert, V., Rioual, S., Le Bozec, N., and Thierry, D., 2022. Corrosion behavior of additively manufactured AISI 316L stainless steel under atmospheric conditions. *Materials and Corrosion,* 73, pp.1833-1843.

Hu, J., Yang, L., Cao, G., Yun, Y., Yuan, G., Yue, Q., and Shao, G., 2016. On the oxidation behavior of (Zr, Nb) 2Fe under simulated nuclear reactor conditions. *Corrosion Science,* 112, pp.718-723.

Hull, F.C., 1967. Effect of delta ferrite on the hot cracking of stainless steel. *WELD Journal,* 46, p.399.

Ida, N., Nishimoto, M., Muto, I., and Sugawara, Y., 2024. Role of MnS in the intergranular corrosion and depassivation of sensitized Type 304 stainless steel. *NPJ Materials Degradation*, 8, p.2.

Kalpakjian, S., and Schmid, S., 2006. Manufacturing, Engineering and Technology SI 6th Edition-Serope Kalpakjian and Stephen Schmid: Manufacturing, Engineering and Technology, Digital Designs.

Le, D., Ji, W., Kim, J., Jeong, K., and Lee, S., 2008. Effect of antimony on the corrosion behavior of low-alloy steel for flue gas desulfurization system. *Corrosion Science*, 50, pp.1195-1204.

Leygraf, C., Graedel, T.E., Tidblad, J., and Wallinder, I.O., 2000. *Atmospheric Corrosion*. Wiley-Interscience, New York.

Liptáková, T., 2009. *Bodová Korózia Nehrdzavejúcich Ocelí (Pitting Corrosion of Stainless Steels)*. EDIS, Žilina.

Maier, B., and Frankel, G., 2010. Pitting corrosion of bare stainless steel 304 under chloride solution droplets. *Journal of The Electrochemical Society*, 157, p.C302.

Maier, B., and Frankel, G., 2011. Pitting corrosion of silica-coated type 304 stainless steel under thin electrolyte layers. *Corrosion,* 67, p.035004-1-035004-10.

Mampuya, M., Umba, M., Mutombo, K., and Olubambi, P., 2021. Effect of heat treatment on the microstructure of duplex stainless steel 2205. *Materials Today: Proceedings,* 38, pp.1107-1112.

Manning, P., Duquette, D.J., and Savage, W.F., 1980. The effect of retained ferrite on localized corrosion in duplex 304L stainless steel. *Weld Journal*, 59, pp.260-262.

Mi, N., 2014. *Synchrotron X-ray Studies of Atmospheric Pitting Corrosion of Stainless Steel.* University of Birmingham, England.

Mi, N., Ghahari, M., Rayment, T., and Davenport, A.J., 2011. Use of inkjet printing to deposit magnesium chloride salt patterns for investigation of atmospheric corrosion of 304 stainless steel. *Corrosion Science,* 53, pp.3114-3121.

Mohammed Ali, H.B., 2016. *Atmospheric Pitting Corrosion of Stainless Steel.* University of Birmingham, England.

Mohammed-Ali, H.B., 2025. Atmospheric pitting corrosion of TIG welded type 316L austenitic stainless steel under MgCl2 droplets. *Corrosion*, 81, pp.492-501.

Mohammed-Ali, H.B., Street, S.R., Attallah, M.M., and Davenport, A.J., 2018. Effect of microstructure on the morphology of atmospheric corrosion pits in type 304L stainless steel. *Corrosion,* 74, pp.1373-1384.

Montoya, T., Katona, R., Karasz, E.K., Taylor, J.M., Snow, J., Bryan, C.R., Kelly, R.G., and Schaller, R.F., 2023. Influence of realistic, cyclic atmospheric cycles on the pitting corrosion of austenitic stainless steels. *Journal of The Electrochemical Society,* 170, p.041502.

Nishimoto, M., Muto, I., and Sugawara, Y., 2023. understanding and controlling the electrochemical properties of sulfide inclusions for improving the pitting corrosion resistance of stainless steels. *Materials Transactions,* 64, pp.2051-2058.

Park, J., Matsch, S., and Böhni, H., 2001. Effects of temperature and chloride concentration on pit initiation and early pit growth of stainless steel. *Journal of the Electrochemical Society,* 149, p.B34.

Ryan, M.P., Williams, D.E., Chater, R.J., Hutton, B.M., and Mcphail, D.S., 2002. Why stainless steel corrodes. *Nature*, 415, pp.770-774.

Schindelholz, E., Risteen, B., and Kelly, R., 2014. Effect of relative humidity on corrosion of steel under sea salt aerosol proxies: II. MgCl2, artificial seawater. *Journal of The Electrochemical Society,* 161, p.C460.

Schmuki, P., Hildebrand, H., Friedrich, A., and Virtanen, S., 2005. The composition of the boundary region of MnS inclusions in stainless steel and its relevance in triggering pitting corrosion. *Corrosion Science,* 47, pp.1239-1250.

Sedriks, A.J., 1996. *Corrosion of Stainless Steels*. John Wiley & Sons, United States.

Standard, A., 2005. Standard guide for examination and evaluation of pitting corrosion.

Street, S.R., Cook, A.J., Mohammed-Ali, H.B., Rayment, T., and Davenport, A.J., 2018. The effect of deposition conditions on atmospheric pitting corrosion location under Evans droplets on type 304L stainless steel. *Corrosion*, 74, pp.520-529.

Street, S.R., Mi, N., Cook, A.J., Mohammed-Ali, H.B., Guo, L., Rayment, T., and Davenport, A.J., 2015. Atmospheric pitting corrosion of 304L stainless steel: The role of highly concentrated chloride solutions. *Faraday Discussions*, 180, pp.251-265.

Tavares, S., Fruchart, D., and Miraglia, S., 2000. A magnetic study of the reversion of martensite α' in a 304 stainless steel. *Journal of Alloys and Compounds,* 307, pp.311-317.

Tsutsumi, Y., Nishikata, A., and Tsuru, T., 2007. Pitting corrosion mechanism of Type 304 stainless steel under a droplet of chloride solutions. *Corrosion Science*, 49, pp.1394-1407.

Van Nam, T., Tada, E., and Nishikata, A., 2015a. Pit initiation and repassivation of stainless steels exposed to cyclic relative humidity changes. *Journal of the Electrochemical Society,* 162, p.C419.

Van Nam, T., Tada, E., and Nishikata, A., 2015b. Pitting corrosion of stainless steel 430 in the presence of thin MgCl2 solution films: Effects of film diameter and thickness. *Materials Transactions,* 56, pp.1219-1225.

Wang, Y., Wang, W., Liu, Y., Zhong, L., and Wang, J., 2011. Study of localized corrosion of 304 stainless steel under chloride solution droplets using the wire beam electrode. *Corrosion Science,* 53, pp.2963-2968.

Webb, E.G., and Alkire, R.C., 2002a. Pit initiation at single sulfide inclusions in stainless steel: I. Electrochemical microcell measurements. *Journal of the Electrochemical Society,* 149, p.B272.

Webb, E.G., and Alkire, R.C., 2002b. Pit initiation at single sulfide inclusions in stainless steel: II. Detection of local pH, sulfide, and thiosulfate. *Journal of the Electrochemical Society,* 149, p.B280.

Williams, D.E., and Zhu, Y.Y., 2000. Explanation for initiation of pitting corrosion of stainless steels at sulfide inclusions. *Journal of The Electrochemical Society,* 147, p.1763.

Zatkalíková, V., and Markovičová, L., 2019. Corrosion resistance of electropolished AISI 304 stainless steel in dependence of temperature. In: *IOP Conference Series: Materials Science and Engineering*. IOP Publishing. p.012011.

Zhang, M.X., Kelly, P., Bekessy, L., and Gates, J., 2000. Determination of retained austenite using an X-ray texture goniometer. *Materials Characterization,* 45, pp.39-49.